

Magnetic-field-induced nonequilibrium structures in a ferrofluid emulsion

George A. Flores and Jing Liu

Department of Physics and Astronomy, California State University, Long Beach, California 90840

M. Mohebi and N. Jamasbi

Center for Scientific Investigation and Higher Education of Ensenada, Ensenada, Baja California, Mexico

(Received 4 June 1998)

Using optical microscopy, we studied magnetic-field-induced structures in a confined ferrofluid emulsion where the magnetic field is applied quickly as a step function. Columnar, bent-wall-like, and labyrinthine structures in three dimensions are observed, corresponding to disks, “worms,” and branchlike patterns in cross-sectional area normal to the magnetic-field direction. These two-dimensional structures are characterized by both the ratio of worms to total aggregates and the average complexity $\langle C \rangle$ of the aggregates in a given image. “Phase” diagrams are obtained to characterize disk (columnar) to worm (bent-wall) structural transitions as a function of the thickness of the cell used to confine the sample along the field direction, the particle volume fraction, and the rate of the magnetic-field application. The distribution of aggregate complexity for a given image is characterized by the skewness and quality factor to describe the symmetry and width of complexity distribution. The results show that increasing either cell thickness L , particle volume fraction Φ , or magnetic field ramping rate R increases the average complexity of the formed patterns as $\langle C \rangle = 1.8\Phi^{3.11}L + 0.141 \log_{10}(R) + 0.83$, as well as the symmetry and the range of the complexity. This relation can be understood qualitatively. For fast ramping rate R or increasing Φ (decreasing the interparticle distance and thus increasing the particle interaction), the strong magnetic interaction between particles does not allow particles enough time to explore the lowest-energy state (columnar structures) before being locked into local energy minima (labyrinthine structures). The L dependence of the complexity supports molecular dynamics simulation results: Chains form first and then aggregate to form complex structures; longer chains have a larger range of attraction. [S1063-651X(99)06301-1]

PACS number(s): 82.70.Kj, 75.50.Mm, 75.70.Kw, 61.30.Eb

I. INTRODUCTION

Magnetorheological (MR) fluids are suspensions of magnetizable particles in a liquid. When a strong magnetic field is applied to a MR fluid, the magnetic dipole moment is induced in each particle. The suspension goes through a structural transition from a gas of randomly dispersed particles to a solid of aggregates of particles. This leads to the rheological change of MR fluids from a liquid to a solid state, which is rapid and reversible. This rheological property is responsible for many current and potential industry applications found in MR fluids ranging from semiactive shock absorbers for automobiles through dampers for mountain bikes, washing machines, and buildings and bridges for seismic damage control to devices for hand exercise in physical therapy [1,2]. The controllable rheological change is due to the particle structures formed by the application of a magnetic field. Therefore, it is important to study the field-induced structures to fully understand the mechanism of the rheology in MR fluids.

From our earlier work, we found that the structures of the solid phase in a model MR fluid (ferrofluid emulsion) can take the form of separated chains, columns, “bent walls” (“worms” when viewed perpendicular to the magnetic field), or labyrinthine patterns depending on the external parameters. These tuning parameters include the strength of the applied field, the ramping rate of the field, the sample confinement along the field direction, and particle volume fractions [3,4].

Due to the difficulty of theoretical modeling, the study of field-induced structures of MR fluids has been limited to the case of an equilibrium state where the external magnetic field is applied slowly enough that particles have time to find the lowest-energy state assisted by the thermal motion [3,5,6]. The equilibrium structure is separate columns with average spacing proportional to the cell thickness along the field direction to a power of 0.37 [5]. Field-induced structures have been studied also under equilibrium conditions in a very similar material, electrorheological fluid, where a dipole moment in each particle is induced by externally applied electric field. Due to the imaging dipoles from conducting boundaries, the equilibrium structure is phase separated into liquid and solid in which particles form a body-centered-tetragonal order [7]. The only field-induced nonequilibrium structures studied so far are in ferrofluid where permanent dipoles are suspended in a liquid with random orientation at room temperature [8,9]. When a big drop of ferrofluid (~ 2 cm, oil based) in water is confined between two glass plates and an external magnetic field is applied normal to the glass surface, a labyrinthine pattern is observed with complexity depending on the rate of field application [9]. In this case, the intrinsic surface tension between the oil-water interface confines the ferrofluid drop and the dipolar force pushes the ferrofluid drop apart. A competition between these two energies underlies the shape evolution. In MR fluids, no aggregation exists without an external field. Therefore, there is no intrinsic surface tension and permanent dipole moment. This makes the modeling and understanding of the nonequilibrium structures of MR fluid more difficult.

Even though to our knowledge, no previous work exists on the study of nonequilibrium structures of induced dipolar fluids, the patterns formed by MR fluid show a similarity to many physical and chemical systems such as ferrofluids [10], type-I superconducting films [11], lipid monolayers [12], and diblock copolymers [13], to name a few. These domain shapes and patterns have raised great interest recently as the phenomenology of modulated phases [14]. They are stabilized by competing interactions and characterized by periodic spatial variations of the pertinent order parameter controlled by temperature and other external fields. Therefore, the study of field-induced structures of MR fluids is interesting from both a basic physics point of view as modulated phases and the understanding of the rheology of MR fluids for applications.

In this paper we report the study of the magnetic-field-induced nonequilibrium structures in a model MR fluid: ferrofluid emulsion. We studied the formation of these patterns by varying the cell thickness L in the field direction, the particle volume fraction Φ of the sample, and the application or ramping rate of the magnetic field $R = dH/dt$ (the slope as in a step function) for a fixed final field strength H_{\max} . Even the slowest rate R (2.4 mT/s) is too fast for the system to reach an equilibrium state. The nonequilibrium structures formed range from separate columns and bent-wall-like to maze structures or labyrinthine patterns. By analyzing the cross-sectional pattern of the three-dimensional (3D) structure at a plane normal to the magnetic-field direction, we quantified changes of the nonequilibrium structures as a function of the three tuning parameters.

Two quantities are introduced to characterize the overall induced structures normal to the field direction: P , the ratio of “worms” to total aggregates, and $\langle C \rangle$, the average complexity. The worm is defined as the ratio of long and short axes of an aggregate that is larger than or equal to 2. The complexity C is defined as the contour of an aggregate relative to that of a disk with the same area. Structural “phase” diagrams are constructed to describe the structural transitions from the regime of column-dominated structures to bent-wall-dominated structures. We take $P = 50\%$ and $\langle C \rangle = 1.50$ as the dividing line between these two regimes. Structural transition relations between L , Φ , and R are obtained quantitatively. This is an extension of our earlier work [4] on the L - Φ relation at a fixed R . The results show that increasing the cell thickness, particle volume fraction, or magnetic-field ramping rate increases the average complexity of the formed patterns as $\langle C \rangle = 1.8\Phi^{3.11}L + 0.141 \log_{10}(R) + 0.83$. Therefore, in tuning the structural complexity, Φ and L are more sensitive parameters than R . In addition, the skewness S and the quality factor Q are used to describe the symmetry and width of the complexity distribution of aggregates for a given image. We found that both S and Q decrease with L and Φ linearly and R logarithmically. That is, as L , Φ , or R increases, the distribution of complexity broadens and becomes more symmetric.

Qualitatively, the dependence of the structure complexity on the tuning parameters can be understood from the time that it takes for the particles to aggregate together, which depends on the ratio of the magnetic interaction energy between particles relative to thermal energy. At fast ramping rate R or increasing Φ (decreasing the interparticle distance

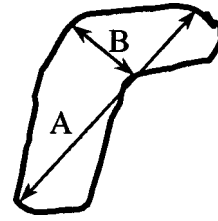


FIG. 1. Typical shape of an aggregate. A and B are the major and minor axes of the aggregate, respectively. A is defined as the maximum end-to-end length of the aggregate and B is defined as the maximum end-to-end length of the aggregate perpendicular to A .

and thus increasing the particle interaction), the strong magnetic interaction between particles does not allow particles enough time to explore the lowest-energy state (columnar structure) before being locked into local energy minima (labyrinthine structures). The L dependence of the complexity suggests a structural formation process that is supported by molecular dynamics simulation: Chains form first limited by the cell thickness and then aggregate to form complex structures. The L dependence also suggests that longer chains have a larger range of attraction, which is confirmed by two-chain models from both simulation and analytical calculation. We hope that this work provides the data with which any theoretical model can be compared.

II. EXPERIMENTAL PROCEDURES AND METHODS FOR DATA ANALYSIS

The ferrofluid emulsion used in this experiment is composed of droplets of ferrofluid coated with sodium dodecyl sulfate surfactant and suspended in water [3]. The ferrofluid consists of 6% by volume of Fe_3O_4 grains of average size 10 nm in kerosene. Those grains are coated with oleic acid to avoid flocculation. The emulsion droplets have an average diameter $2a$ of $0.27 \mu\text{m}$ with a polydispersity of about 20%. The samples were sealed with petroleum gel in glass capillary cells, which have a typical length of 4 cm and a rectangular or square cross section $W \times L$. Here the thickness L along the direction of the field and the width W is typically $10L$ for a rectangular cell.

Optical microscopy is used to study the induced structures [4]. The sample cell sits on top of a stage on a Nikon inverted optical microscope where a coil is used to produce a dc magnetic field normal to the viewing plane and the surface of the cell. A charge-coupled device camera is attached to the microscope to capture images, which are sent to a computer for storage and analysis. A program called SIGMASCAN is used to calculate each aggregate’s area, perimeter, and major and minor axes.

Figure 1 sketches a typical aggregate (called a worm) in a given image from the top view. The images captured after the structures reach a steady state are analyzed by determining the complexity in terms of the parameters P and $\langle C \rangle$, defined below. To calculate P , we first measure the aspect ratio e of an aggregate defined as the ratio of the major axis A to the minor axis B of the aggregate. SIGMASCAN defines the major axis as the longest end-to-end distance of a given aggregate and the minor axis as the longest end-to-end distance of the aggregate perpendicular to the major axis [Fig. 1 and Eq. (1a)]. If $e \geq 2.0$, the aggregate is defined as a worm.

If $e < 2.0$, the aggregate is defined as being disklike. We then define P as the ratio of the number of worms to the total number of aggregates N_t for a given image. We take $P = 50\%$ as the transition between disks and worms in a 2D image. Since the definition of minor axis is good only for an ellipse, this quantity P works well for characterizing patterns near the beginning of the transition, where most aggregates are disks and ellipses with $e \sim 2-4$ and very few aggregates are bent or have multiple arms:

$$e = \frac{L_{\text{maj}}(A)}{L_{\text{min}}(B)}, \quad P = \frac{N_{e \geq 2}}{N_t}, \quad (1a)$$

$$C = \frac{\mathcal{P}}{2\sqrt{\pi A}}, \quad \langle C \rangle = \frac{\sum_{i=1}^{N_t} C_i}{N_t}, \quad (1b)$$

where L_{maj} denotes the major axis length, L_{min} the minor axis length, \mathcal{P} the perimeter of the aggregate, and A the area of the aggregate.

To characterize aggregates with shapes more complex than disks and ellipses, the complexity C is used. C is defined as the ratio of the perimeter of an aggregate to the perimeter of a disk with the same area, as shown in Eq. (1b). If an aggregate is a perfect disk, $C = 1.0$. If the aggregate has multiple arms, C is greater than 1.0; the larger the C , the more complex the aggregate. Once we calculated the values for each aggregate in a given image of a total number of N_t , we then average C over the whole image to obtain the average complexity $\langle C \rangle$. We take $\langle C \rangle_T = 1.5$ as the dividing line between columns and bent walls to find quantitative relations among the parameters L , Φ , and R .

These definitions of $P_T = 50\%$ and $\langle C \rangle_T = 1.5$ are arbitrarily chosen. One may set different values to P_T and $\langle C \rangle_T$, which would define different structural transitions. For a worm with an elliptical shape, $e = 2$ corresponds to $C = 1.01$. If a structure with $P = 50\%$ consists only of disks and ellipses with $e \sim 2$, then $\langle C \rangle$ would be 1.005, which is not a sensitive parameter. We have found that $\langle C \rangle = 1.5$ corresponds to $P = 50\%$ for our images. Therefore, the structure is more complex than just disks and ellipses; $\langle C \rangle$ is a better quantity than P to be used for characterizing most of our structures. For comparison purpose, we kept P as well.

Previously only P was used to characterize the induced patterns, while L and Φ were varied at a single field ramping rate R [4]. In this work, we vary all three parameters R , L , and Φ and use both P and $\langle C \rangle$ to characterize the induced structures. In all the experiments, the maximum magnetic field H_{max} is fixed at 24.0 mT for simplicity. The coupling constant λ , defined as the dipolar interaction energy of two dipoles aligned head to tail over the thermal energy of the system, is calculated to be 74 [5]. One may also vary H_{max} which is not done in our present work. The droplet volume fraction Φ of the sample ranges from 0.04 to 0.14, the sample cell thickness L ranges from 20 to 1000 μm , and the applied magnetic field rate R ranges from 2.40 to 400.0 mT/s. The latter rate corresponds to a rise time of 60 ms in an exponentially increasing field, which is limited by the response of the current supply and the magnetic coil. The longest time taken to ramp the field from 0 to 24.0 mT is 10

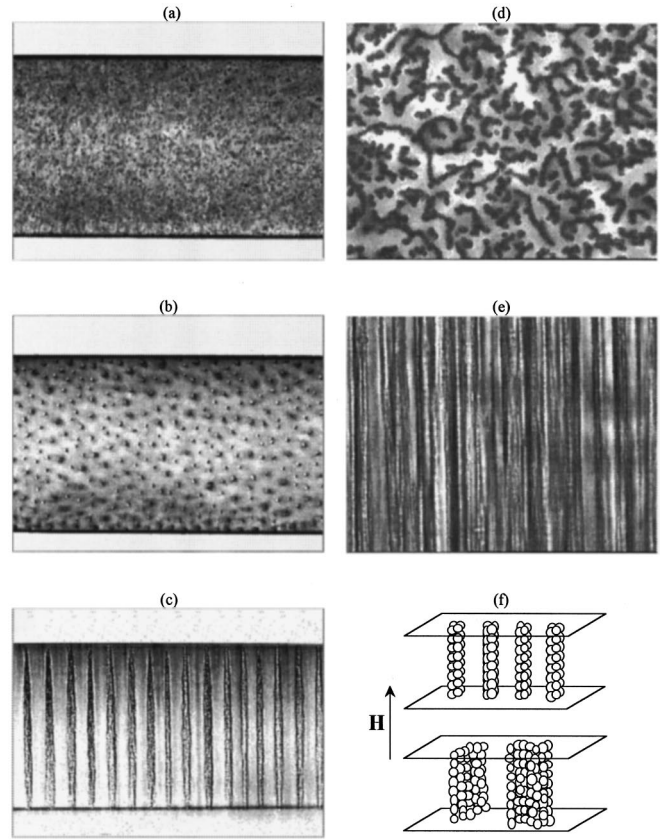


FIG. 2. Images showing the formation of ferrofluid structures. (a) Droplets with no applied magnetic field. (b) and (c) Columnar solid structure shown from the top and side views formed at $L = 50 \mu\text{m}$, $\Phi = 0.03$, and $R = 400.0 \text{ mT/s}$. (d) and (e) Bent-wall-like solid structure shown from the top and side views formed at $L = 200 \mu\text{m}$, $\Phi = 0.10$, and $R = 400.0 \text{ mT/s}$. (f) 3D comparison of the reconstructed columnar solid structure formed with a slow ramping rate and bent-wall-like solid structure formed with a high ramping rate. Image widths are $80 \mu\text{m}$.

s, which is linearly increased by hand. In all cases, it takes from a fraction of a second to a minute for the structure to reach a steady state, depending upon L , Φ , and R .

III. RESULTS

A. Induced nonequilibrium structures

In the absence of any external magnetic field, the droplets of the sample are randomized due to Brownian motion. The sample is in a ‘‘gaseous’’ state [15]. When an external magnetic field is applied to the ferrofluid emulsion, randomly dispersed Brownian droplets aggregate to form three-dimensional solid structures. At a low R , the solid structure is equally spaced columns with equal width, which shows plan symmetry perpendicular to the applied field direction. The top view shows a pattern with separate disks [3,5]. However, when R is high, the shapes of the aggregates become more complex. The solid structure appears as a ‘‘folded sheet’’ or a bent wall. It is wormlike from the top view, which becomes a maze or labyrinthine pattern if R increases further [4].

Figure 2 shows typical microscopic images of columnar and bent-wall patterns from both top and side views. Figure

2(a) shows the gas structure without an applied field. After the magnetic field is applied, at low L , Φ , and R , the steady state structure is locally ordered columns as shown in Figs. 2(b) and 2(c) of the same structure viewed from the top and side. At high L , Φ , and R , the saturated pattern from the top view is a mixture of disks and worms reflecting columnar and bent-wall structures in three dimension as shown in Figs. 2(d) and 2(e) from the top and side views. Figure 2 illustrates that the chain formation is the basis for aggregates. Even in the labyrinthine pattern, the side view shows straight chains joined to form a maze structure. However, not all the chains have equal length and fill the cell gap (L) completely. To better illustrate the aggregates in three dimensions, Fig. 2(f) shows the reconstructed structures discussed earlier for both low and high sets of L , Φ , and R parameters.

For a quantitative study, all the patterns are captured at the end of the cell nearest to the objective lens of the microscope for clear image. From Fig. 2, the 2D pattern at different cross sections along the magnetic-field direction is the same for columnar structures and can be different for labyrinthine structures where not all chains have equal length and are linked equally throughout the entire cell along L as shown in Fig. 2(e). When we focused on different cross sections in the sample (limited to the first 100 μm by using an oil-immersed objective lens), we found very small overall differences in terms of the complexity, although each aggregate at a different position along L in the image may be different. Nevertheless, readers should keep in mind that the 2D patterns have limitations in studying the 3D structures.

The pattern shown in Fig. 2(d) is very similar to those observed in ferrofluids [8] where a big drop of ferrofluid (2.1 cm) in water is confined between two glass plates and the external magnetic field is applied normal to the glass surface. As the field strength increases, a labyrinthine pattern develops. Depending on the rate of the field application, the number of arms evolved from the drop varies. In this case, the intrinsic surface tension between the oil-water interface plays a key role in confining the ferrofluid drop and the dipolar force pushes the ferrofluid drop apart. A competition between these two energies underlies the shape evolution. Our ferrofluid emulsion system does not have any intrinsic surface tension; droplets coated with surfactant do not aggregate without an external magnetic field. To make an analogy to the patterns formed by the ferrofluid drop, we need to assume that an induced surface energy from the magnetic field competes with the induced repulsive energy between dipoles. These two energies, along with the geometric constraint, set the many local energy minima that determine the shape of the structures formed. The surface energy has been used to calculate equilibrium structures of induced dipolar fluids [5,6,16]. It originates from the different local magnetic fields (due to demagnetization) experienced by particles at the surface and the inside of an aggregate. Therefore, it is possible that the underlying physics of the pattern formation is similar to that of the ferrofluid. To understand the structure fully, a nonequilibrium dynamics calculation is needed.

Figure 2 illustrates the influence of all three parameters upon the complexity of the structure formation. If we vary only one parameter at a time, say, Φ , and keep the other two parameters constant, similar disk-worm transitions can be produced as well. Varying either L or R has a similar effect

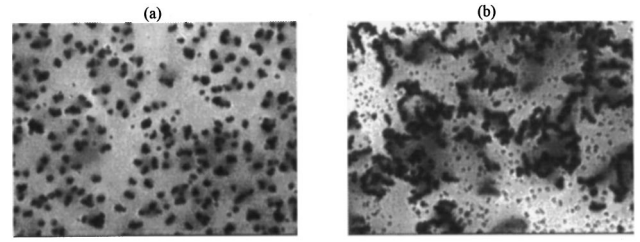


FIG. 3. Microscopic images of formed patterns from the top view taken at $H_{\text{max}}=24.0$ mT for different parameters: (a) $L = 1000$ μm , $\Phi = 0.04$, and $R = 400.0$ mT/s, where $P_T = 12.8\%$ and $\langle C \rangle_T = 1.2$, and (b) $L = 1000$ μm , $\Phi = 0.065$, and $R = 400.0$ mT/s, where $P_T = 54.2\%$ and $\langle C \rangle_T = 1.7$. The horizontal width of each image is 80 μm .

[4]. Figures 3(a) and 3(b) show a comparison of microscopic images for different Φ from the top view below and above the transition line of $P_T = 50\%$ and $\langle C \rangle_T = 1.50$ at $L = 1000$ μm and $R = 400.0$ mT/s. At $\Phi = 0.04$ [Fig. 3(a)], we see that the image is predominantly disks reflecting 3D columnar structures. These disks show short-range order and have a narrow size distribution close to the saturated equilibrium structures [5]. When Φ is increased to 0.065, Fig. 3(b) shows an image that is now predominantly worms. This image contains various structures ranging from single particles (chains in three dimensions) through disks, simple ellipses, and random worms to aggregates with multiple arms.

B. Quantitative analysis of structures and structural phase transition diagrams

To analyze the images in Figs. 3(a) and 3(b), we first characterize each aggregate with values of e and C defined in Eq. (1). The distribution of both e and C over the whole image in Figs. 3(a) and 3(b) is then plotted as a histogram in Fig. 4; Figs. 4(a) and 4(b) correspond to Fig. 3(a) and Figs. 4(c) and 4(d) correspond to Fig. 3(b). Each image has typically 100–1000 aggregates, which gives reasonable statistics. The bin width for these histograms is 0.05. The solid lines in Fig. 4 are fits of the Gaussian distribution. Increasing the volume fraction from 0.04 to 0.065 not only changes $\langle C \rangle$ from 1.19 to 1.62 but also changes the distribution of C as seen by comparing Figs. 4(a) and 4(c). Similarly, Φ also changes the average e from 1.19 to 2.41 and the distribution, shown in Figs. 4(b) and 4(d). P is calculated using Eq. (1a).

It is clear from the above images that to capture every detail requires more parameters than $\langle C \rangle$. Let us first focus on P and $\langle C \rangle$ only and leave their distributions to a later section. From the histograms, the parameters P and $\langle C \rangle$ characterizing the complexity are calculated. We then vary Φ and continue the same process to obtain a series of P and $\langle C \rangle$. From these data, P vs Φ and $\langle C \rangle$ vs Φ are then plotted as shown in Figs. 5(a) and 5(b), where $L = 800$ μm and $R = 400.0$ mT/s. From the curve fit (solid line) and setting $P_T = 50\%$ and $\langle C \rangle_T = 1.5$ as our criteria for the transition from column to bent-wall structures, the corresponding structural transition parameter Φ_T is then found separately for P and $\langle C \rangle$. The same procedures and criteria are used to find the transition parameter L_T at $R = 400.0$ mT/s and $\Phi = 0.10$, as shown in Figs. 5(c) and 5(d), and R_T at $L = 200$ μm and $\Phi = 0.12$, as shown in Figs. 5(e) and 5(f). Structural phase

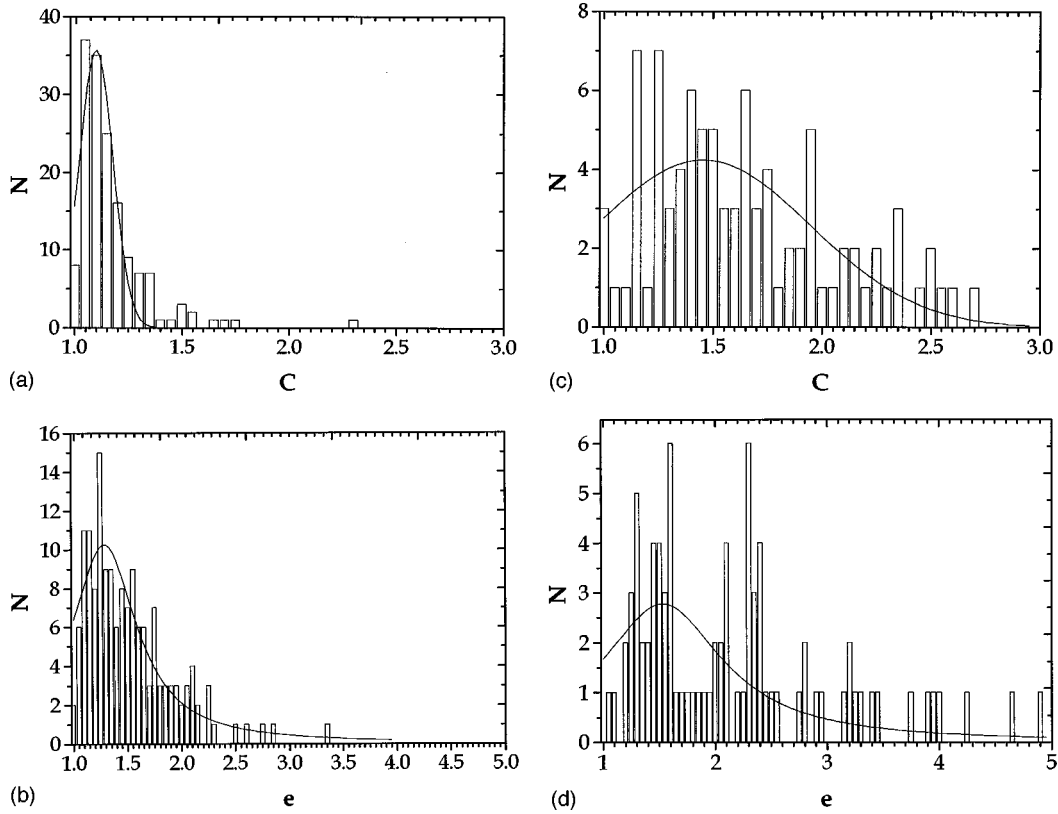


FIG. 4. Histogram plots of Fig. 3 showing the distribution of the aggregate number N as a function of complexity C and worm ratio e . (a) and (b) correspond to Fig. 3(a) and (c) and (d) correspond to Fig. 3(b).

diagrams are then constructed for any two of the three parameters.

It is interesting to notice from Fig. 5 that P and $\langle C \rangle$ vary linearly with Φ and L but logarithmically with R for the range of L , Φ , and R measured:

$$\langle C \rangle = 1.21 + 0.0014L, \quad (2a)$$

$$\langle C \rangle = 0.332 + 17.2\Phi, \quad (2b)$$

$$\langle C \rangle = 1.31 + 0.141 \log_{10}(R). \quad (2c)$$

Here the range of L or R varies about one order of magnitude and Φ only 0.02. As our earlier work shows [4], if Φ is varied over one order of magnitude, P increases with Φ as a power law with an exponent in the range 2.2–2.9. We have tried the power-law fitting to Figs. 5(a) and 5(b); only small differences in Φ_T are seen due to the small range of Φ varied. In our earlier work, when R is varied over four orders of magnitude, P increases with R still logarithmically. A molecular dynamics simulation [17] also shows the same logarithmic dependence of $\langle C \rangle$ on R :

$$\langle C \rangle = 1.01 + 0.195 \log_{10}(R). \quad (2d)$$

Here the coupling constant is 139, $\Phi = 0.1$, $2a = 0.2 \mu\text{m}$, $L = 8 \mu\text{m}$, and a cell size of $1 \mu\text{m} \times 1 \mu\text{m} \times 8 \mu\text{m}$ is used. The different coefficients between Eqs. (2c) and (2d) may be due to the different coupling constant used in computer simulation (139) compared to that in experiment (76) and the limited cell size in the simulation. In the simulation, the chain formation is about 10 times faster than the chain aggregation.

The fact that Eq. (2d) agrees well with the experimental results of Eq. (2c) indicates that the dipole-dipole interaction in a chain formation is stronger than the chain-chain interaction in an aggregate formation.

The results of Fig. 5 may be summarized in one equation

$$\langle C \rangle = a_1 \Phi^\alpha L + a_2 \ln(R) + a_3, \quad (3)$$

where α and a_i are constants that should be a function of the applied magnetic field, particle susceptibility, and size. These constants can be determined by obtaining additional relations between Φ , L , and R and by setting $\langle C \rangle = \text{const}$. It is clear from Eq. (3) that L and Φ are more sensitive parameters than R for their effect on tuning the structure complexity.

By setting $\langle C \rangle_T = 1.5$ and $P_T = 0.5$, Figs. 6(a)–6(c) show the experimentally obtained phase diagrams of the structural transition. Here we measured structural transitions for different pairs of the three parameters while keeping the third parameter constant.

The transition lines divide the space into a bent-wall-dominated region (above them) and a column-dominated region (below them). The farther above the transition lines, the more complex the structure. The farther below the transition lines, the closer the structure to the equilibrium columnar solid. These diagrams show that to obtain a particular worm pattern, we can increase the cell thickness, the particle volume fraction, or the field application rate (also the field strength, if we like).

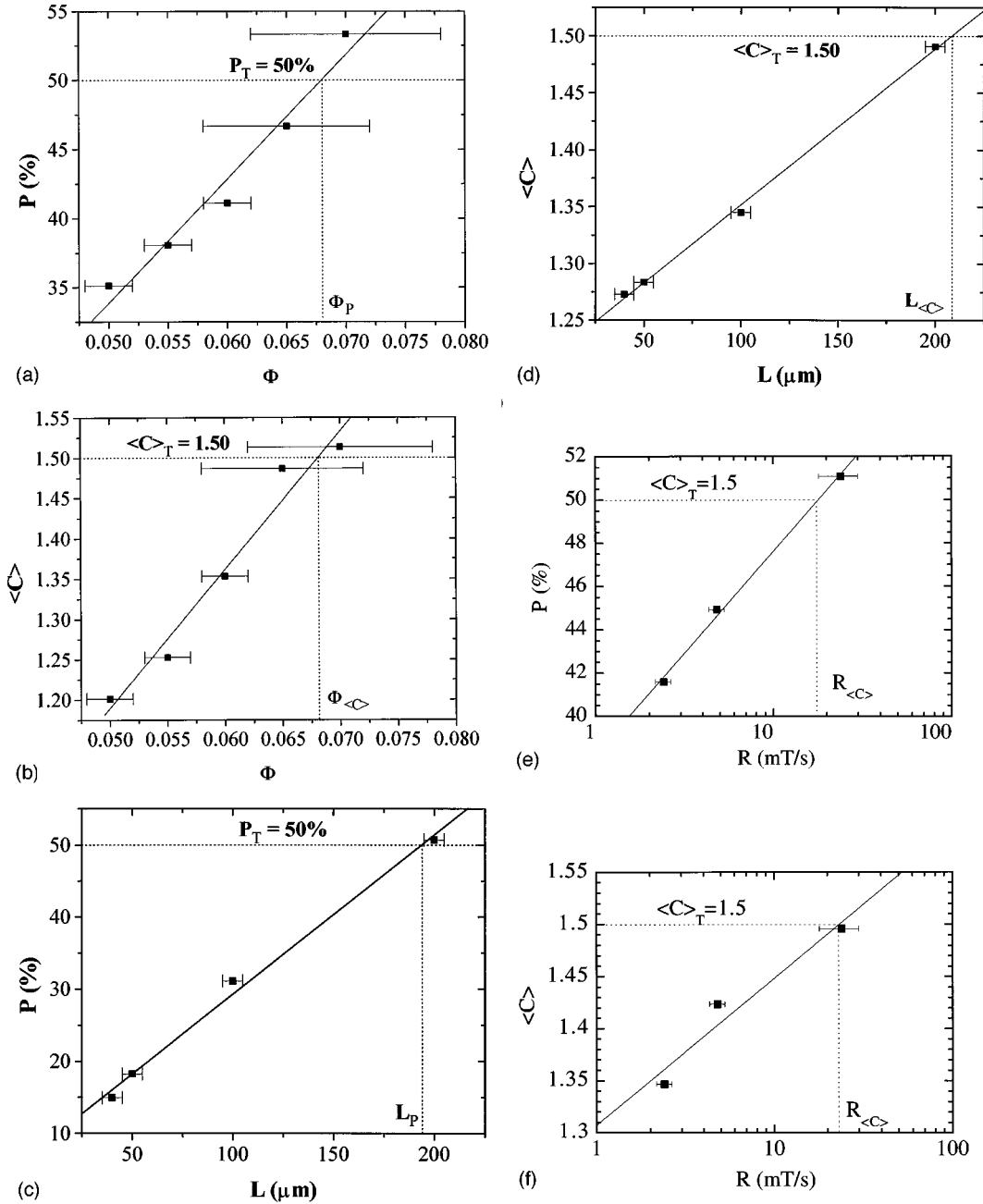


FIG. 5. Relations of P and $\langle C \rangle$ obtained as a function of (a) and (b) Φ at $L=800 \mu\text{m}$ and $R=400.0 \text{ mT/s}$, (c) and (d) L at $R=400.0 \text{ mT/s}$ and $\Phi=0.10$, and (e) and (f) and R at $L=200 \mu\text{m}$ and $\Phi=0.12$. Solid lines show the fits of the data. Dashed lines show the transition parameters defined by setting $P_T=50\%$ and $\langle C \rangle_T=1.50$.

Figure 6(a) shows the transition relation between R_T and L_T at $\Phi=0.10$. The solid and dashed lines are curve fits of the functions

$$R_T = 1779 \exp(-0.0075L_T) \text{ mT/s for } P_T, \quad (4a)$$

$$R_T = 1675 \exp(-0.0074L_T) \text{ mT/s for } \langle C \rangle_T. \quad (4b)$$

They show nearly identical exponential relations. Figure 6(b) shows the transition relation between R_T and Φ_T at $L=200 \mu\text{m}$. The solid and dashed lines are curve fits of the functions

$$R_T = (5.3 \times 10^3) \exp(-7.3 \times 10^3 \Phi_T^{3.48}) \text{ mT/s for } P_T, \quad (4c)$$

$$R_T = (9.5 \times 10^3) \exp(3.7 \times 10^3 \Phi_T^{3.11}) \text{ mT/s for } \langle C \rangle_T. \quad (4d)$$

Again, they show similar fits of complicated exponential functions. Figure 6(c) shows the transition relation between L_T and Φ_T at $R=400.0 \text{ mT/s}$. The solid and dashed lines are curve fits of the functions

$$L_T = 0.071 \Phi_T^{-3.48} \mu\text{m for } P_T, \quad (4e)$$

$$L_T = 0.16 \Phi_T^{-3.11} \mu\text{m for } \langle C \rangle_T. \quad (4f)$$

They also show similar fits of the power-law functions.

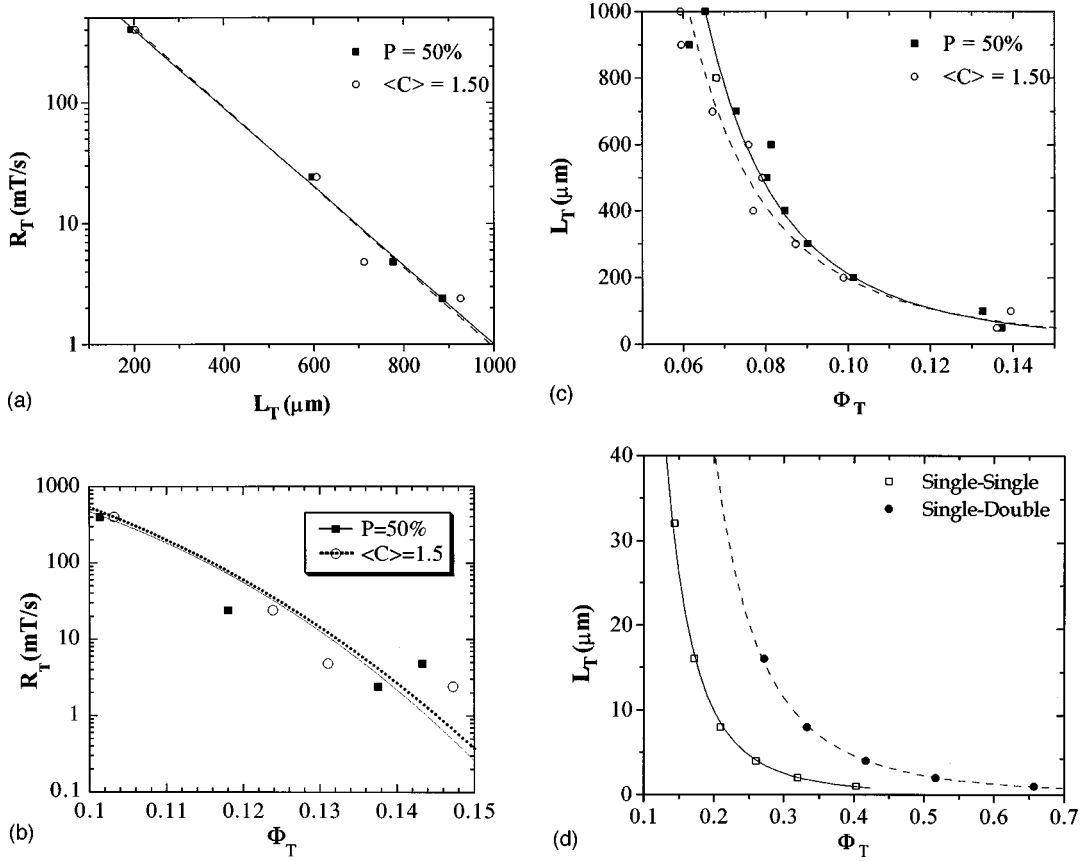


FIG. 6. Structural transition “phase” diagram at $P_T=50\%$ and $\langle C \rangle_T=1.50$. Solid and dashed lines are fits of the data for P_T and $\langle C \rangle_T$, respectively, which separate a transition from column (below the line) to bent-wall (above the line) structures for the (a) R - L relation at $\Phi=0.10$, (b) R - Φ relation at $L=200 \mu\text{m}$, and (c) L - Φ relation at $R=400.0 \text{ mT/s}$. (d) Computer simulation for single chains to a two-chain column (squares) and single, double chains to a three-chain column (closed circles) transitions, where solid and dashed lines are power-law fits.

As we expect from Eq. (3) for transitions (setting $\langle C \rangle = \text{const}$ and $P = \text{const}$), a power-law relation exists between L_T and Φ_T and exponential relations exist between R_T and L_T and between R_T and Φ_T . Even though simple exponential functions of $R_T = (3 \times 10^7) e^{-113\Phi_T}$ for P_T and $R_T = (8 \times 10^7) e^{-121\Phi_T}$ for C_T also fit well the data shown in Fig. 6(b) as our other paper shows [18], more complicated exponential functions as shown in Eqs. (4c) and (4d) are used to take into account data from both Figs. 5 and 6. Combining Eqs. (2)–(4), the constants in Eq. (3) are thus determined:

$$\langle C \rangle = 1.8\Phi^{3.11}L + 0.141 \log_{10}(R) + 0.83. \quad (5)$$

Equation (5) confirms that a master relation exists between the average complexity and the three tuning parameters.

As shown from these plots in Fig. 6, P_T and $\langle C \rangle_T$ exhibit similar behavior as L , Φ , and R are varied. At the transition lines, according to our definition $P_T=50\%$, the structures comprise one-half disks and one-half worms. If the worms were ellipses only, $e=2$ would give $C=1.01$ not $C=1.5$. The fact that $\langle C \rangle_T=1.5$ while $P=50\%$ suggests that the worms are either characterized by $e=10$ or are far from ellipses. In the latter case, aggregates at the transition lines must have a wide distribution of shapes and a fraction of them having curved worm shape and multiple arms dominates the value of $\langle C \rangle$. This is consistent with direct observation in Fig. 3 and with the histograms shown in Fig. 4.

Figure 6(d) shows computer simulation results with curve fits obtained on the basis of two-chain (open squares and solid line) and three-chain (closed circles and dashed line) interactions. The escape distance of two chains or three chains, within which the chains aggregate to form a column and above which the chains stay separated, were found for a given chain length L by molecular dynamics simulation performed at zero temperature for our sample condition [19]. The escape distance is then converted to the particle volume fraction Φ to obtain the data in Fig. 6(d), assuming that all chains have the same length L and are arranged in a hexagonal-close-packed lattice. Therefore, the solid curve indicates the structural transition from single chains to a column consisting of double chains, whereas the dashed curve indicates the structural transition from a mixture of single and double chains to columns consisting of three chains in a row. On the solid curve, any two single chains will have a 50% chance of aggregating or staying separate. If we use the parameter $P = N^{\text{column}}/N_{\text{total}}$ to characterize the structure, we will have $P=50\%$ at the solid line and $P=67\%$ at the dashed line. If we use the complexity $\langle C \rangle$ to define the transition line as used in our earlier definition, we find that $\langle C \rangle = 1.2$ at the solid line for the transition of C from 1 to 1.4 and that $\langle C \rangle = 1.38$ at the dashed line for the transition of C from 1.2 to 1.73. Obviously, if we want to make a more precise comparison with the experimental data, we need to

consider $\langle C \rangle = 1.5$ for the interaction among multiple chains at room temperature.

Even though the above model is a crude one for the chain aggregation process, the simulation does predict very interesting transition relations from the curve fitting results:

$$L_T = 0.045 \Phi_T^{-3.35} \mu\text{m} \quad \text{for } \langle C \rangle = 1.2, \quad (6a)$$

$$L_T = 0.26 \Phi_T^{-3.14} \mu\text{m} \quad \text{for } \langle C \rangle = 1.38. \quad (6b)$$

The relations are very close to the experimental result $L_T = 0.16 \Phi_T^{-3.11} \mu\text{m}$ obtained for $\langle C \rangle_T = 1.5$. From the fact that only small difference exists in the power-law relation between the exponents obtained for $\langle C \rangle = 1.2$ and $\langle C \rangle = 1.38$, we expect that the exponent will still be greater than 3 at $\langle C \rangle = 1.5$. Experimentally, we have checked transitions for $P = 40\%$ and 60% from the data used to obtain Fig. 6(c). Similar power-law $L_T - \Phi_T$ relations were found in which the exponent increases slightly (8%) as P increases from 40% to 60%. To a first-order approximation, all the transition lines arising from different definitions of P_T are essentially parallel [4]. Therefore, the simple model of the two- or three-chain interaction can give a good approximation to the transition relation for more complicated structures.

The success of the simple model of simulation in predicting the $L_T - \Phi_T$ relation at the fast ramping rate ($R = 400.0$ mT/s) suggests a simple picture of the nonequilibrium structural formation process: Separate chains form first and then these chains aggregate to form columns through a direct interaction. The thermal-fluctuation-induced long-range interaction between chains is not important in the chain aggregation process here as it might be in the equilibrium state [20].

C. Qualitative understanding of the structural transition phase diagrams

Even though simulation predicted successfully the relations of Eqs. (4f) and (2c), no analytical theory exists so far to explain quantitatively the master relation in Eq. (5). Qualitatively, we can understand the dependence of the complexity of structures on the three parameters through the time that it takes for the particles to aggregate. In an equilibrium state where the field is applied very slowly, the induced structures are separate columns. In a nonequilibrium state where the field is applied quickly, the structures formed are more complex. Let us look at the R dependence for two extreme cases. At low R , the dipoles induced in the droplets are weak enough so that the droplets can still move about exploring the lower-energy states before they are locked by strong dipole forces at high H , corresponding to $\lambda \sim 5$ based on experimental observation. In this case, the particles are packed densely into columnar structures to reduce the total energy consisting of demagnetization energy, repulsive energy between the ends of columns, and the surface energy [5,6,15,16]. At large R and high H , the dipoles induced in the droplets are very strong right after the field is applied so that the attraction between neighboring droplets and chains pulls them together without allowing the time to explore the lowest-energy state. The bent-wall structures correspond to metastable states in which the structures are locked into one of the local minima. The process is analogous to quenching a

simple liquid to a solid by reducing temperature. Fast cooling results in a glass structure, whereas slow cooling generally results in a crystal structure.

The effect of the particle volume fraction can be understood on the basis of the same consideration. At a higher Φ , the droplets are closer to each other and the dipoles interact strongly for the same field. Therefore, the particles link more quickly. The faster the linkage, the more complex the structure and the farther away from the equilibrium state. At low Φ , not only is the separation between droplets large so that the dipolar force is small, but also the fluid viscous and thermal forces will slow down the droplet motion. These forces give the droplets more time to explore the lower-energy states.

The L dependence of the complexity suggests a structural formation process: Chains form first limited by the cell thickness and then aggregate to form complex structures. However, it is not clear why the induced structures become more complex as the cell thickness increases. To understand this, we have done a computer simulation [17,19], which confirmed that the structure formation proceeds in two steps: chain formation and chain aggregation. The formation of chains that touch the boundary is about ten times faster than the aggregation of chains for $L = 40$ ($2a$) at both $T = 0$ and 300 K and at large R . Since a complex pattern arises from a quick aggregation that originates from a strong dipolar attraction, the experimental results ($\langle C \rangle \sim L$) suggest that the interaction between long chains is stronger than that between short chains. This is confirmed by molecular dynamics simulation of the two-chain model where the chains have a relative shift of one particle radius: The chain-chain attractive range increases with the chain length as $r_e \sim L^\alpha$ for $0 < L \leq 200$ ($2a$), where $\alpha = 0.15$ for $T = 0$ K and $\alpha = 0.2$ for $T = 300$ K ($\lambda = 139$) [17,19]. The power-law relation is also confirmed by analytical calculations for two chains having equal length and one particle radius shift, where $\alpha = 0.19$ at $\lambda = 10$ for $0 < L \leq 3000$ ($2a$) and $\alpha = \frac{1}{3}$ at $\lambda = \infty$ for $L \geq 1000$ ($2a$) [21,22].

Although the chain attractive range increases with the chain length corresponding to our experimental cell range from 2.2 at $L = 70$ ($2a$) to 5.1 at $L = 3000$ ($2a$) based on the result of the above analytical calculation at $\lambda = 10$, the increase in the interaction range slows down when chains are more than 200 particle diameters. The two-chain interaction model alone may not be sufficient to count for the complex structures formed in larger cells. We believe that the labyrinthine pattern observed in thicker cells [$L > 200$ ($2a$)] may come from complicated interactions between long chains, long and short chains, chains with different relative shift along the chain direction, and multiple-chain interactions simultaneously. A heterogeneous chain length is possible because the chain formation is a very quick process with its length depending on the local particle density distribution. The large cells allow the particle density to fluctuate more and therefore different chain lengths form. This heterogeneous chain interaction could increase the attractive range r_e further and therefore result in more complicated structures.

We can also understand the large interaction range for long chains from the following simple physical pictures. The ends of chains having like poles repel each other, which plays an important role in the equilibrium structure forma-

tion [3,5]. The shorter the chains, the stronger the effect of repulsion from the ends on chain aggregation. As a result, long chains will attach to each other at their middles and zip through the rest of the chains. They tend to form aggregates with chains of slightly different lengths and relative shifts. In equilibrium columnar structures, we found either tapered ends or split ends of columns, reflecting the effect of repulsion between ends [3]. The same repulsion of ends may also affect the formation of nonequilibrium structures.

The simulation of the two-chain interaction shows that temperature increases the range of attraction between the two chains, but not that the attraction between two chains depends on the chain length. The fact that Eq. (6b) agrees quite well with Eq. (4f) shows that the temperature is not crucial in the chain aggregation in the case of a fast ramping rate. A direct interaction between chains is the dominant factor for chain aggregation. For a slow ramping rate to reach equilibrium state, the formation of the columnar structure depends strongly on the temperature for thermal motion to bring the particles to the lowest-energy state. Therefore, a thermal-induced chain fluctuation could be important in equilibrium chain aggregation [15,20].

D. Structural complexity distribution

So far, we have used P and $\langle C \rangle$ to understand the structure transition. We have found that the distribution of C is also very interesting. To analyze the complexity distribution shown in Fig. 4, we have introduced two new parameters: the *skewness* S and the *quality factor* Q .

S is a dimensionless quantity that measures how much asymmetry, or shift from center, occurs in the distribution of the complexity. The standard definition for S is given as

$$S = \frac{\sum_{i=1}^{N_t} \left(\frac{C_i - \langle C \rangle}{\sigma} \right)^3}{N_t} \quad \text{where } \sigma = \sqrt{\frac{\sum_{i=1}^{N_t} (C_i - \langle C \rangle)^2}{N_t - 1}}. \quad (7)$$

Here N_t is the total aggregates for a given image and σ is the standard deviation of the complexity.

The *quality factor* Q measures how narrow the distribution of complexity is. It is defined as

$$Q = \frac{C_{\max}}{\Delta C_{\text{FWHM}}}, \quad (8)$$

where C_{\max} is the maximum value of the Gaussian fit of the histogram and ΔC_{FWHM} is the full width at half maximum. For an RC circuit, Q measures how many cycles this system would oscillate before it dampens out. The higher the Q , the more cycles the signal oscillates. In our case, the higher the Q , the narrower the distribution of aggregate complexity.

For a symmetric distribution of N vs C , S is zero. If $S > 0$, the N - C distribution peak goes to the left of $\langle C \rangle$. If $S < 0$, the peak will go to the right of $\langle C \rangle$. In our data, we found that S is always larger than zero. This means that those aggregates with $C_i > \langle C \rangle$ weigh more in a given image, spreading out more toward larger C . In all the data, $Q > 1$ also. There is always a peak found in the N - C distribution.

Figure 7(a) shows the case for $S \gg 0$ ($S = 2.31$, Q

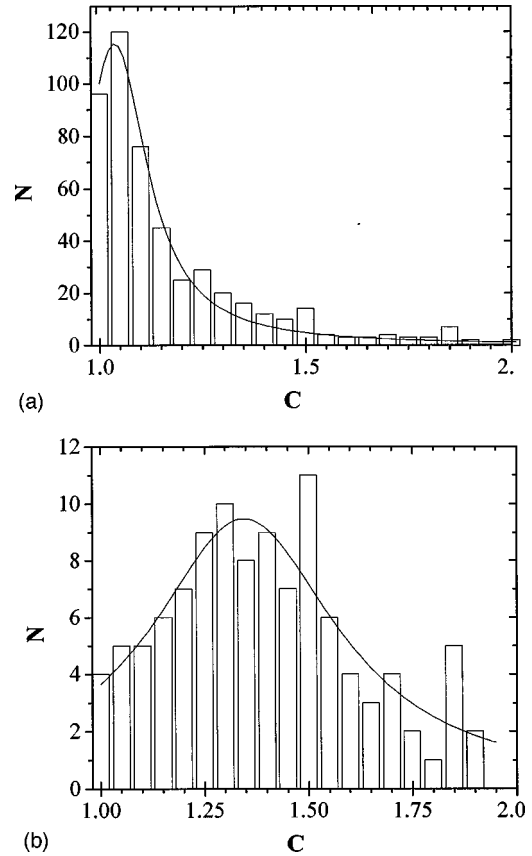
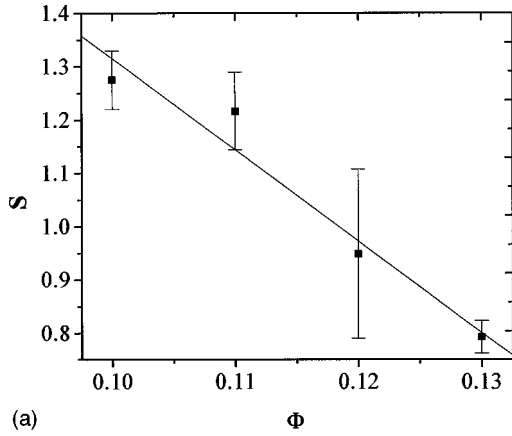


FIG. 7. Aggregate number vs complexity distribution showing the progression toward symmetry as L increases from (a) $L = 300 \mu\text{m}$, where $\langle C \rangle = 1.37$, $S = 2.31$, and $Q = 766.7$, to (b) $L = 500 \mu\text{m}$, where $\langle C \rangle = 1.42$, $S = 0.21$, and $Q = 13.83$. For both cases, $\Phi = 0.10$ and $R = 24.0 \text{ mT/s}$ and solid lines are fits of Gaussian distributions.

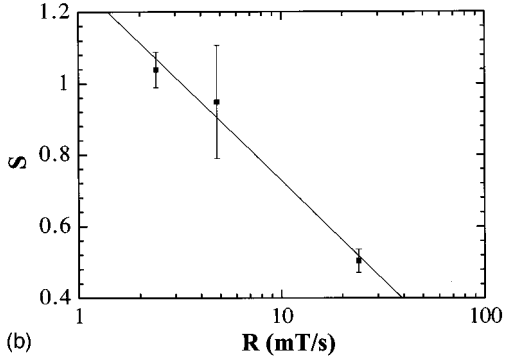
$= 766.7$, and $\langle C \rangle = 1.37$), where $L = 300 \mu\text{m}$, $\Phi = 0.10$, and $R = 24.0 \text{ mT/s}$. The N - C distribution peak is shifted toward smaller values of C from $\langle C \rangle$. In other words, we have more aggregates that are columnar than bent-wall-like and the bent-wall-like structures can transform to a quite complex shape. At the same time, the distribution is quite narrow as the Q value shows. As L increases to $500 \mu\text{m}$ while keeping Φ and R constant, Fig. 7(b) shows that S decreases by a factor of 10 while the average complexity increases slightly ($S = 0.21$, $Q = 13.83$, and $\langle C \rangle = 1.42$). The distribution of the number of columns and bent walls is nearly symmetric and broad.

As shown in Fig. 7 and our other data, for low values of L , Φ , or R while $\langle C \rangle$ is normally low, S and Q are both quite high. This means that besides a predominant number of columnar aggregates with narrow distribution, small amounts of bent-wall aggregates also exist. As L , Φ , or R increases to increase $\langle C \rangle$, S and Q begin to decrease. This means that for predominantly bent-wall aggregates, the distribution of the aggregates is more widely spread and symmetric. Therefore, it seems that a correlation between $\langle C \rangle$ and S , Q (the symmetry and width of the complexity C) exists.

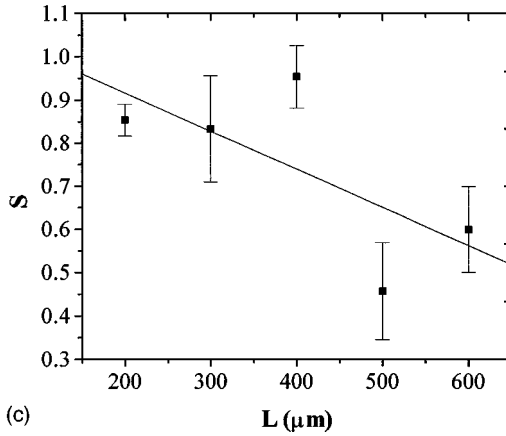
Let us now examine the dependence of S and Q on each parameter separately. Figures 8(a)–8(c) show S as a function of Φ , R , and L and Figs. 9(a)–9(c) show Q as a function of Φ , R , and L . As Φ increases while R and L are fixed at



(a)



(b)



(c)

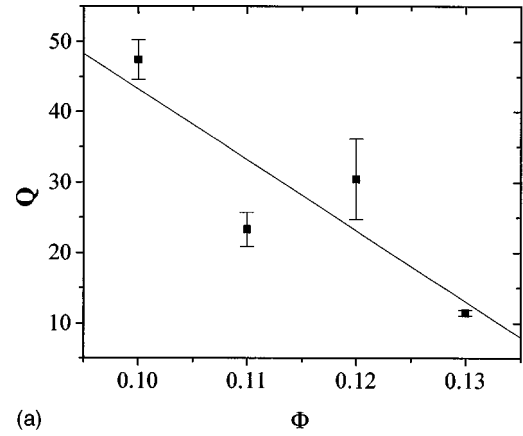
FIG. 8. Skewness S in the Gaussian distribution to measure the symmetry of the aggregate distribution as a function of (a) Φ at $R = 4.80$ mT/s and $L = 200$ μm , (b) R at $L = 200$ μm and $\Phi = 0.12$, and (c) L at $R = 24.0$ mT/s and $\Phi = 0.10$. The solid line is the best fit for (a) $S = 3.03 - 17.15\Phi$, (b) $S = 1.28 - 0.55 \ln(R)$, and (c) $S = 1.09 - 0.00088L$.

$R = 4.8$ mT/s and $L = 200$ μm , Figs. 8(a) and 9(a) show that S and Q decrease with Φ as

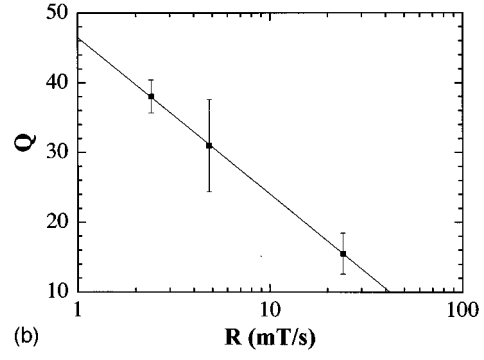
$$S = 3.03 - 17.15\Phi, \quad (9a)$$

$$Q = 144.06 - 1008\Phi. \quad (9b)$$

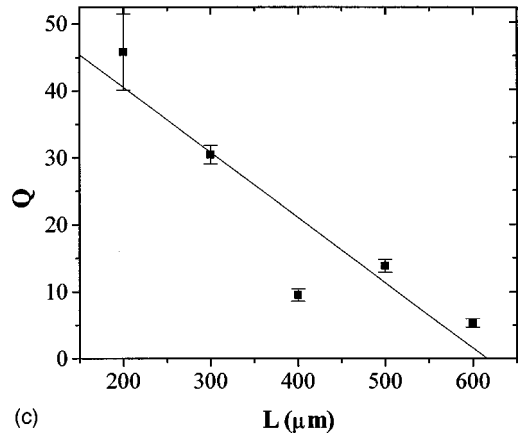
In other words, higher concentration of particles gives a structure more complex and its distribution more symmetric



(a)



(b)



(c)

FIG. 9. Quality factor Q to measure the width of aggregate distribution as a function of Φ , R , and L with the same condition as in Fig. 8. The solid line is the best fit for (a) $Q = 144.06 - 1008\Phi$, (b) $Q = 46.45 - 22.4 \ln(R)$, and (c) $Q = 59.98 - 0.097L$.

and broader. As R increases while L and Φ are fixed at $L = 200$ μm and $\Phi = 0.12$, Figs. 8(b) and 9(b) show that S and Q decrease with R as

$$S = 1.28 - 0.55 \log_{10}(R), \quad (9c)$$

$$Q = 46.45 - 22.4 \log_{10}(R). \quad (9d)$$

Increasing both Φ and R results in a more symmetric and broad distribution of aggregates while increasing the average complexity $\langle C \rangle$. Finally, as L increases while R and Φ are fixed at $R = 24.0$ mT/s and $\Phi = 0.10$, Figs. 8(c) and 9(c) show that S and Q decrease with L as

$$S = 1.09 - 0.00088L, \quad (9e)$$

$$Q = 59.98 - 0.097L. \quad (9f)$$

It is interesting that the dependence of S and Q on either L or Φ is a linear function, but on R it is logarithmic. This is similar to the results for the structural transition as shown in Fig. 5. The complexity and its distribution (symmetry and width) depend more sensitively on L and Φ than on R . As the range of Φ increases, the S, Q dependence on Φ may also change from linear to a power-law function. The exact relation can be understood only if we have a model. We hope that this work will provide the basis for any theoretical models for comparison.

IV. CONCLUSIONS

This study shows that by applying an external magnetic field to a ferrofluid emulsion, different structures can be induced from separate chains and columns through bent walls to labyrinths. The existence of many different patterns indicates a complicated energy map induced in the system, with many local minima that sensitively depend on the set of parameters such as R , H_{\max} , L , and Φ . Columnar structures are induced if particles are allowed to explore their lower-energy states before settling down. Complex bent-wall structures are created if the particles are locked into aggregates by a strong dipolar interaction that is too quick for particles to explore the lower-energy states.

The complexity of the induced structures are controlled by a set of parameters R , H_{\max} , L , and Φ . Increasing either one of them increases the complexity of the structure as well

as the width and symmetry in the complexity distribution. Transitions between different structures are possible by adjusting one or more of these parameters. The column to bent-wall transition is continuous over a large range of these parameters. If we define $P_T = 50\%$ and $\langle C \rangle_T = 1.50$ as the columns to bent-wall transition lines, structural phase diagrams can be constructed for pairs of these parameters. A simple relation between the tuning parameters are found as $\langle C \rangle = 1.8\Phi^{3.11}L + 0.141 \log_{10}(R) + 0.83$. Φ and L are more sensitive parameters than R in tuning the structures. The cell thickness dependence of the complexity of the patterns indicates that the formation of chains is the first step in forming aggregates. Longer chains have a larger attractive range between chains. A direct interaction is important in chain aggregation to form nonequilibrium structures.

This work forms the basis for building theoretic models for understanding the mechanism of the dipole interaction in nonequilibrium states. The microscopic structure controls the rheological properties of the fluids. As our recent rheological study [23] shows, the yield stress is stronger when an equilibrium structure is formed as compared to a nonequilibrium structure for the same sample and field strength. Characterizing induced structures in MR fluids can provide useful information for optimizing the rheological properties.

ACKNOWLEDGMENTS

We thank Dr. Mark Gross and Dr. Serge Cutillas for helpful discussions. This work was partially supported by grants from NASA (Grant No. NAG3-1830), the NSF (DMR Grant No. 9321201), the Exxon Educational Foundation, and California State University, Long Beach.

-
- [1] J. D. Carlson, D. M. Catanzarite, and K. A. St. Clair, in *Proceedings of the Fifth International Electrorheological and Magnetorheological Fluid Conference, Sheffield, 1995*, edited by W. Bullough (World Scientific, Singapore, 1996).
- [2] J. D. Carlson and B. F. Spencer, Jr., in *Proceedings of the Third International Conference on Motion and Vibration Control, Chiba, 1996*, edited by K. Nanomi and T. Mizuno (Japan Society of Mechanical Engineers, Tokyo, 1996), Vol. III, p. 3540.
- [3] J. Liu, E. M. Lawrence, M. L. Ivey, G. A. Flores, J. Bibette, and J. Richard, in *Proceedings of the Fourth International Conference on Electrorheological Fluids, Feldkirch, 1993*, edited by R. Tao (World Scientific, Singapore, 1994).
- [4] G. A. Flores, M. L. Ivey, J. Liu, M. Mohebi, and N. Jamasbi, *Int. J. Mod. Phys. B* **10**, 3283 (1996).
- [5] J. Liu, E. M. Lawrence, A. Wu, M. L. Ivey, G. A. Flores, K. A. Javier, J. Bibette, and J. Richard, *Phys. Rev. Lett.* **74**, 2828 (1995).
- [6] E. Lemaire, Y. Grasselli, and G. Bossis, *J. Phys. II* **2**, 359 (1992); E. Lemaire, G. Bossis, and Y. Grasselli, *ibid.* **4**, 253 (1994).
- [7] R. Chen, R. N. Zitter, and R. Tao, *Phys. Rev. Lett.* **68**, 2555 (1992).
- [8] R. E. Rosensweig, *Ferrohydrodynamics* (Cambridge University Press, Cambridge, 1985); *Sci. Am.* **247** (10), 136 (1982).
- [9] A. J. Dickstein, S. Erramilli, R. E. Goldstein, D. P. Jackson, and S. A. Langer, *Science* **261**, 1012 (1993); D. P. Jackson and R. E. Goldstein, *Phys. Rev. E* **50**, 298 (1994).
- [10] F. Elias, C. Flament, J. Bacri, and S. Neveu, *J. Phys. I* **7**, 711 (1997).
- [11] R. P. Huebener, *Magnetic Flux Structures in Superconductors* (Springer-Verlag, Berlin, 1979).
- [12] K. Y. C. Lee and H. M. McConnell, *J. Phys. Chem.* **97**, 9532 (1993).
- [13] M. W. Matsen and M. Schick, *Phys. Rev. Lett.* **72**, 2660 (1994).
- [14] M. Seul and D. Andelman, *Science* **267**, 476 (1995).
- [15] Y. Zhu, M. L. Ivey, P. Pousset, and J. Liu, *Int. J. Mod. Phys. B* **10**, 2973 (1996).
- [16] W. Toor and T. C. Halsey, *Phys. Rev. A* **45**, 8617 (1992).
- [17] M. Mohebi, N. Jamasbi, G. Flores, and J. Liu, in *Proceedings of the Sixth International Conference on Electrorheological Fluids, Magnetorheological Suspensions and Their Applications, Yonezawa, 1997*, edited by K. Koyama and M. Nakano (World Scientific, Singapore, in press).
- [18] G. A. Flores, J. Liu, M. Mohebi, and N. Jamasbi, in *Proceedings of the Sixth International Conference on Electrorheological Fluids, Magnetorheological Suspensions and Their Applications, Yonezawa, 1997* (Ref. [17]).
- [19] M. Mohebi, N. Jamasbi, and J. Liu, *Phys. Rev. E* **54**, 5407 (1996).

- [20] T. C. Halsey and W. Toor, *J. Stat. Phys.* **61**, 1257 (1990).
- [21] M. Gross and S. Kiskamp, *Phys. Rev. Lett.* **79**, 2566 (1997).
- [22] M. Gross, S. Kiskamp, H. Eisele, and J. Liu, in *Proceedings of the Sixth International Conference on Electrorheological Fluids, Magnetorheological Suspensions and Their Applications*, Yonezawa, 1997 (Ref. [17]).
- [23] Y. Zhu, M. McNeary, N. Breslin, and J. Liu, in *Proceedings of the Sixth International Conference on Electrorheological Fluids, Magnetorheological Suspensions and Their Applications*, Yonezawa, 1997 (Ref. [17]).